Materials Science & Engineering A 918 (2024) 147446

Contents lists available at ScienceDirect

Materials Science & Engineering A

journal homepage: www.elsevier.com/locate/msea

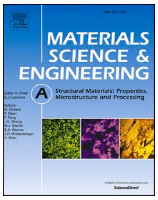

Mechanical properties of pure elements from a comprehensive first-principles study to data-driven insights

Shun-Li Shang [a,b,*], Michael C. Gao [b], Yi Wang [a,b], Jingjing Li [c], Allison M. Beese [a,d], Zi-Kui Liu [a]

[a] Department of Materials Science and Engineering, The Pennsylvania State University, University Park, PA, 16802, USA
[b] Computational Science Engineering Directorate, National Energy Technology Laboratory, Albany, OR, 97321, USA
[c] Department of Industrial and Manufacturing Engineering, The Pennsylvania State University, University Park, PA, 16802, USA
[d] Department of Mechanical Engineering, The Pennsylvania State University, University Park, PA, 16802, USA

ARTICLE INFO

Keywords:
Mechanical properties of pure elements
Correlation analysis
Density functional theory
Pure alias shear deformation
Pure tensile deformation

ABSTRACT

Unraveling mechanical properties from fundamental is far from complete despite their vital role in determining applicability and longevity for a given material. Here, we perform a comprehensive study related to mechanical properties of 60 pure elements in bcc, fcc, hcp, and/or diamond structures by means of pure alias shear and pure tensile deformations via density functional theory (DFT) based calculations alongside a broad review of existing literature. The present data compilation enables a detailed correlation analysis of mechanical properties, focusing on DFT-based ideal shear and tensile strengths (τ_{is} and σ_{it}), stable and unstable stacking fault energies (γ_{sf} and γ_{us}), surface energy (γ_s), and vacancy activation energy (Q_V); and experimental hardness (H_B), ultimate tensile strength (σ_{UT}), fracture toughness (K_{Ic}), and elongation (ε_{EL}). The present work examines models, identifies outliers, and provides insights into mechanical properties, for example, (i) H_B is correlated by Q_V, σ_{UT} by $\sqrt{\gamma_s}$ or $\sqrt{\gamma_{us}}$, and K_{Ic} by γ_s; (ii) data outliers are identified for Cr (related to τ_{is}, γ_s, Q_V, and σ_{UT}), Be (τ_{is}, γ_{sf}, γ_{us}, and Q_V), Hf (H_B and K_{Ic}), Yb (all properties), and Pt (γ_{sf} vs. γ_{us}); and (iii) τ_{is}, σ_{it}, γ_{sf}, γ_{us}, γ_s, Q_V, and H_B are highly correlated to elemental attributes, while σ_{UT}, K_{Ic}, and especially ε_{EL} are less correlated due mainly to experimental uncertainty. In particular, the present data compilation provides a solid foundation to model properties such as γ_s and τ_{is} of multicomponent alloys and τ_{is} of unstable structures like bcc Ti, Zr, and Hf.

1. Introduction

Mechanical properties describe the range of usefulness and the expected service life of a material, and help classify and identify materials [1–3]. They typically include hardness, yield strength, ductility, and fracture toughness, which measure the resistances of materials to deformation, cracking, and/or fracture under an applied load. Mechanical properties can be modelled through deformation mechanisms in terms of fundamental materials properties [2]; see the 19 empirical models summarized in Table 1 [1,4–20]. These models are also the key resources to design new features (descriptors) to correlate mechanical properties; see Sec. 2.2. Table 1 shows that elastic properties of bulk modulus (B) and shear modulus (G) are closely related to ideal shear strength (ISS or τ_{is}; see the model #1 in Table 1) [4], unstable stacking fault energy (USFE or γ_{us}; model #3) [13], Peierls stress (σ_P; model #5) [15], hardness (model #8) [18], plane strain fracture toughness (e.g., the critical stress intensity factor K_{Ic} under the Mode-I loading condition; models #10 to #12) [5,13,20], and ductility (models #13, #15, and #16) [1,6,8,9]. Table 1 also indicates that mechanical properties can be tailored by local properties relevant to a given surface or interface such as surface energy (γ_s), stable and unstable stacking fault energies (γ_{sf} and γ_{us}), and the associated derivatives of ideal shear and ideal tensile strengths (τ_{is} and σ_{it}). For example, γ_{us} can be regulated by τ_{is} (the model #2 in Table 1) [13], σ_{it} by γ_s (model #4) [14], σ_P by τ_{is} (model #5) [15], the ability of plastic deformation and the emission of a partial dislocation by γ_{sf} and γ_{us} (models #6 and #7) [16,17], yield stress σ_y by γ_{us} (model #9) [19], and fracture toughness by γ_s and γ_{us} (models #10 and #11) [5,13,20]. Regarding ductility or brittleness for a given material, Table 1 summarizes that it can be qualitatively predicted using the global materials properties via Pugh's ratio (B/G) [6], Cauchy pressure ($C_{12} - C_{44}$ with C_{ij} being the elastic constants) [10], valence electron concentration (VEC) [11], and electron work function (EWF) [12], and

---

* Corresponding author. Department of Materials Science and Engineering, The Pennsylvania State University, University Park, PA, 16802, USA.
E-mail address: sus26@psu.edu (S.-L. Shang).

https://doi.org/10.1016/j.msea.2024.147446
Received 22 July 2024; Received in revised form 20 October 2024; Accepted 21 October 2024

Table 1
Empirical models to tailor mechanical properties in the literature.

Properties	Relationships with references[a]	No.
ISS (τ_{is})	$\tau_{is} = \left(\frac{Gb}{2\pi h}\right)$ [4]	1
USFE (γ_{us})	$\gamma_{us} = (b\tau_{is}/3.125)$ [13]	2
	$\gamma_{us} = \left(Gb^2/2\pi^2 h\right)$ [13]	3
ITS (σ_{it})	$\sigma_{it} = \sqrt{E\gamma_s/h}$ [14]	4
Peierls stress (σ_P)	$\sigma_P = \frac{2G}{1-\nu}\exp\left(\frac{-4\pi\zeta}{b}\right)$ [15]	5
Ability of plastic deformation (γ_d)	$\gamma_d = \gamma_{sf}/\left(\gamma_{us} - \gamma_{sf}\right)$ [16]	6
Emission of a partial dislocation (β)	$\beta = \left(1 - \gamma_{sf}/\gamma_{us}\right)$ [17]	7
Hardness (H_V for Vickers)	$H_V \propto \left(G^3/B^2\right)$ [18]	8
Yield stress (σ_y)	$\sigma_y = \left(\frac{4\gamma_{us}}{0.31b} + \frac{\tau_0}{0.31}\right)$ [19]	9
Fracture toughness (critical stress intensity factor under, e.g., the Mode-I loading condition, K_{Ic})	$K_{Ic} \propto \sqrt{2G\gamma_{us}/(1-\nu)}$ [13]	10
	$K_{Ic} = \sqrt{4\gamma_s G/(1-\nu)}$ [5,20]	11
	$K_{Ic} = \left((1+\alpha)V_0^{1/6}G(B/G)^{1/2}\right)$ [5]	12
Ductility or brittleness	Pugh's ratio: B/G [6]	13
	Rice's ratio: γ_s/γ_{us} [13]	14
	KTC criterion: τ_{is}/σ_{it} [7] ($\propto G/\sqrt{E}$) [1]	15
	RT criterion: Gb/γ_s [8,9]	16
	Cauchy pressure: $(C_{12} - C_{44})$ [10]	17
	Valence electron concentration (VEC) [11]	18
	Electron work function (EWF) [12]	19

[a] B is the bulk modulus, G the shear modulus, E the Young's modulus, ν the Poisson's ratio, b the Burgers vector, h the interplanar spacing (e.g., between slip planes), γ_s the surface energy, γ_{sf} the stable stacking fault energy (SFE), γ_{us} the unstable stacking fault energy (USFE), α the factor depended on Fermi level, C_{ij} the elastic constants, ζ the dislocation width related to τ_{is} and/or C_{ij} [15], and τ_0 the imposed stress [19].

also using the local materials properties through Rice's ratio (γ_s/γ_{us}) [13], Kelly-Tyson-Cottrell (KTC) criterion (τ_{is}/σ_{it}) [7], and Rice-Thomson (RT) criterion (Gb/γ_s with b being Burgers vector) [8,9].

Table 1 reveals the critical role of fundamental materials properties in determining mechanical properties. It is expected that when all fundamental data are available, it is possible to perform data-driven study of mechanical properties. Especially the data of pure elements are essential to model property ϕ for a given phase using, e.g., the general CALPHAD (calculations of phase diagram) approach starting from unary, binary, ternary, to multicomponent system [21,22]. The property ϕ is usually expressed by the following Redlich-Kister (R-K) polynomial [23],

$$\phi = \phi_0 + \phi_{conf} + \sum_i \sum_{j>i} x_i x_j \sum_{L=0}^{L} \phi_{ij}^{(L)} \left(x_i - x_j\right)^L + \sum_i \sum_{j>i} \sum_{k>j} x_i x_j x_k \phi_{ijk} + \dots \quad \text{Eq. 1}$$

where $\phi_0 = \sum_i x_i \phi_{0,i}$ is the rule-of-mixture approach used frequently in the literature [24], representing mechanical additions of individual properties $\phi_{0,i}$ (e.g., the properties of pure elements) according to their composition x_i. ϕ_{conf} is configurational contribution for some properties such as Gibbs energy. $\phi_{ij}^{(L)}$ and ϕ_{ijk} are the binary and ternary interaction parameters, respectively, with L in parentheses being the label only. The superscript L of $\left(x_i - x_j\right)$ indicates its power, and the subscripts i, j, and k represent different components.

Through the use of density functional theory (DFT) based first-principles calculations, many properties of pure elements have been predicted such as elastic properties (e.g., B, G, and C_{ij}) [25], surface energy (γ_s) [26–28], vacancy activation energy (VaQ or Q_V) [29], lattice stability between different structures [29,30], and various quantities related to lattice parameters (e.g., equilibrium volume V_0 and Burgers vector b) [25,29] for pure elements in bcc, fcc, and hcp structures. However, fewer efforts have been made by DFT-based calculations relevant to tensile and shear deformations, and correspondingly fewer fault energies (e.g., γ_{sf} and γ_{us}) and ideal strengths (τ_{is} and σ_{it}) have been reported in the literature even for pure elements; see the literature data summarized in the supplementary Table S 3 and Table S 4. Besides their roles in modeling mechanical properties (Table 1), γ_{sf}, γ_{us}, τ_{is}, and σ_{it} become more vital to understand and design nanoscale materials and devices, for example, the ultrahigh-strength materials [31] and the packaging materials for electronic devices [32]. Note that γ_{sf} and γ_{us} are key characteristics on the generalized stacking fault energy curve (or the γ-surface) — a measure of energy penalty by shearing two adjacent planes [33,34]. γ_{sf} and γ_{us} can be used to understand and predict a vast number of material properties relevant to dislocations, plastic deformation, crystal growth, and phase transitions [33,34]. Beyond mechanical properties, fundamental properties such as γ_s and Q_V can also be used to understand and predict materials' behaviors related to, e.g., surface structure, defects, and catalysis [35–40] and high energy ball milling [41].

In addition to the examples in Table 1, a lower γ_{sf} corresponds to a large distance between dislocation partials, a higher twin propensity, and a reduced steady-state creep rate [42,43]. It was also proposed that γ_{us} can be used to analyze twinnability [44] and hardness [1], and $\sqrt{\gamma_{us}}$ can be used to study dislocation nucleation at a crack tip [13]. The ideal strengths (τ_{is} and σ_{it}) set the upper bounds on the attainable stresses, which are achievable in nanostructured materials with less or no dislocations; see the measured τ_{is} values of pure elements using nanoindentation and micropillar compression as summarized in the supplementary Table S 3. In particular, τ_{is} is closely related to the minimum stress needed to plastically deform a perfect single crystal (cf., the model #5 in Table 1) and the formation of a stacking fault [33,45].

The present work aims to study mechanical properties through data-driven approaches. *First,* we create a complete dataset of pure elements using digital data from the literature and the present DFT calculations via the pure alias shear [33,34,46] and the pure tensile deformations (to predict γ_{sf}, γ_{us}, τ_{is}, and σ_{it}). *Second,* we perform data-enabled correlation analyses to examine existing models and their application ranges (see Table 1) and gain new insights. *Finally,* as an application of the present data compilation, we model materials properties in bcc-based multicomponent alloys (demo using γ_s and τ_{is}) and unstable phases (demo using Ti, Zr, and Hf in bcc structure).

2. Methods

2.1. DFT-based pure shear and tensile deformations

Four fundamental materials properties τ_{is}, γ_{sf}, γ_{us}, and σ_{it} of pure elements have been predicted in the present work using DFT-based first-principles calculations in terms of the pure alias shear deformation for τ_{is}, γ_{sf}, and γ_{us} [33,34,45–47] and the pure tensile deformation for σ_{it}. Here, the pure deformation refers to full relaxions of atomic positions, cell shape, and cell volume of the structure except for the fixed shear angle or the fixed tensile length. The alias shear involves only one deformed atomic plane, while the degrees of freedom related to the other parts of the supercell remain unchanged [33,34,45–47]. During the pure alias shear deformation, the displacement propagates through the supercell starting from the shear plane due to the interaction between the atoms during shear process, making this process (i) closer to the actual shear situation than such as the affine shear, the simple shear, and the slab shear with more shear assumptions as discussed in details in the literature [33,45,47], and (ii) depicting underlying physics such as the splitting of dislocation into partials [33,45,47]. In addition, the alias shear deformation employs only half atoms without vacuum layers in the supercell in comparison with the slab model [34], making the alias shear computationally efficient to study shear-related properties such as the generalized stacking fault energy curve and the associated τ_{is}, γ_{sf}, and γ_{us} [45].

During the pure alias shear and the pure tensile deformations, the deformed matrix $\overline{\mathbf{R}}$ of lattice vectors can be expressed as [33,34,45],

$$\overline{\mathbf{R}} = \mathrm{RD} \qquad \text{Eq. 2}$$

where **R** is the original, undeformed matrix of lattice vectors and **D** the deformation matrix. All the **D** matrices and the employed orthorhombic supercells in the present work are listed in Table S 6. For the bcc structure, its deformation can be described as the "pencil glide" on any planes containing the $\langle 111\rangle$ direction, with the commonly shear being on the slip systems of $\{1\bar{1}0\}\langle 111\rangle$, $\{11\bar{2}\}\langle 111\rangle$, and $\{12\bar{3}\}\langle 111\rangle$ [48,49]. For the fcc structure, the well documented slip is on the close packed plane and along the close packed direction, i.e., $\{111\}\langle 11\bar{2}\rangle$ [33,47,48]. For the hcp structure, the slip system is $\{0001\}\langle 10\bar{1}0\rangle$ similar to that of fcc plus the other commonly observed slip system of the prismatic $\{10\bar{1}0\}\langle 11\bar{2}0\rangle$ [50,51]. For the diamond structure, its slip systems are similar to those in the fcc structure [1] with the two slip systems $\{111\}\langle 11\bar{2}\rangle$ and $\{111\}\langle 1\bar{1}0\rangle$ used in the present work. Table S 6 summarizes all these slip systems. For the bcc-based binary alloy, we employed three 4-layer, 24-atom special quasirandom structures (SQS's) generated by the ATAT code [52], with each of the pure alias shear deformations performed on each of the four layers; resulting in 12 shear deformations for each concentrated alloy.

Both the pure alias shear and the pure tensile deformations were carried out by an external Python optimizer GADGET developed by Bučko et al. [53] to control DFT-based calculations of stresses and forces acting on each atom. All DFT-based first-principles calculations in the present work were performed using the Vienna Ab initio Simulation Package (VASP) [54] together with the ion-electron interaction described by the projector augmented wave (PAW) method [55] and the exchange-correlation functional described by the generalized gradient approximation (GGA) [56]. In VASP calculations, the electron configurations for each element were the same as those used by the Materials Project [27]. The automatic, instead of the fixed, k-point meshes were used to sample the Brillouin zone in terms of the assigned R_k values (listed in Table S 6) by considering the changes of lattice vectors during shear and tensile deformations. For example, the length of $R_k = 30$ was used to determine the three subdivisions of k-point meshes ($\mathrm{N}_1 \times \mathrm{N}_2 \times \mathrm{N}_3$) for the 24-atom bcc supercells. The VASP setting of "PREC = high" was used to determine the plane-wave basis set. For example, it results in a plane-wave cutoff energy which is 1.3 times the default one. In addition, the ferromagnetic (FM) configurations were used for elements Cr, Mn, Fe, Co, and Ni, except for the antiferromagnetic (AFM) configuration used for bcc Cr. More details and settings regarding the pure alias shear calculations can be found in our previous publications [33,34,45,57].

2.2. Features and data-enabled correlation analyses

Correlation analyses were performed for 10 properties of pure elements, i.e., τ_{is}, γ_{us}, γ_{s}, Q_{V}, σ_{it}, and γ_{sf} from DFT and H_{B}, σ_{UT}, K_{Ic}, and $\varepsilon_{\mathrm{EL}}$ from experiments, in terms of the MATLAB (R2023a) using machine learning (ML) algorithms and elemental properties as features [42,57]. The selection of features was based on (i) the filter-type method of linear fitting to rank individual features and (ii) the sequential feature selection (SFS) method to choose a set of the combined features by means of the linear support vector machine (SVM1) method to avoid overfitting the datasets with large uncertainties (for properties σ_{UT}, K_{Ic}, and $\varepsilon_{\mathrm{EL}}$) or the quadratic SVM (SVM2) method for the datasets with small uncertainties (for properties τ_{is}, γ_{us}, γ_{s}, Q_{V}, σ_{it}, and H_{B}). Iterations between the selected features using the SVM-based SFS method and the ML-based verifications by SVM were detailed previously [42]. For each property, the 5-fold cross validation (CV) method with 500 or 1000 times ML trainings was used for all the SFS processes, the final verifications, and the determinations of data outliers and standard deviations with the details described previously [42].

Elemental properties available in the literature were included as features [42,57], such as the quantities related to periodic table, electronic structures, atomic sizes (volumes), physical properties, thermochemical properties, and elastic properties with details explained in Table S 2 and their values given in the supplemental Excel file. According to the empirical relationships in Table 1, seventeen features were designed and listed in Table S 2, including B/G (#80), G/b (#81), $\sqrt{B/\mathrm{G}}$ (#86), $V_0^{1/6}G(B/G)^{1/2}$ (#88), Gvoigt (#89), Greuss (#92), $\sqrt{\gamma_s G/(1-\upsilon)}$ (#94), $\sqrt{2G\gamma_{\mathrm{us}}/(1-\upsilon)}$ (#95), $\sqrt{\gamma_{\mathrm{us}}}$ (#96), and Gb/γ_{s} (#98). Features connected to each of the 10 properties are given in the supplemental Excel file with the list of sheets in the Excel file presented in Table S 1.

3. Results and discussion

All digital data used in the present work are provided in the supplementary Excel file with 14 sheets as explained in Table S 1 and each individual or designed feature/descriptor described in Table S 2. Other DFT and experimental τ_{is} and γ_{us} values in the literature are given in Table S 3 and Table S 4, respectively. In the present work, the units are GPa for τ_{is} and σ_{it}; J/m^2 for γ_{sf}, γ_{us}, and γ_{s}; eV for Q_{V}; MPa for H_{B} and σ_{UT}; MPa.m$^{1/2}$ for K_{Ic}; and % for $\varepsilon_{\mathrm{EL}}$. The lower values of τ_{is} and γ_{us} are selected for each element in the present work when applicable.

Using those data, correlation analyses are performed for the properties of pure elements in stable and metastable bcc, fcc, hcp, and/or diamond structures with phase stability determined by the positive-definite matrix of elastic constants [25], including (1) DFT-based predictions of ideal shear strength (ISS or τ_{is}, calculated by the present pure alias shear method), ideal tensile strength (ITS or σ_{it}, by the present pure tensile method), stable stacking fault energy (SFE or γ_{sf}, by the present pure alias shear method), unstable stacking fault energy (USFE or γ_{us}, by the present pure alias shear method), surface energy (γ_{s}, in the literature [26,27]), and vacancy activation energy (Q_{V}, in the literature [29]); and (2) experimental properties of hardness (Brinell hardness H_{B}), ultimate tensile strength (σ_{UT}), the average relative elongation ($\varepsilon_{\mathrm{EL}}$) for annealed samples measured at room temperature (e.g., 293 K) when possible [58], and the average fracture toughness (K_{Ic}) based on the AZoM [59].

The detailed analyses are given in Sec. 3.2.1 for τ_{is} and γ_{us}, Sec. 3.2.2 for σ_{it} and γ_{sf}, Sec. 3.3.1for H_{B} and σ_{UT}, and Sec. 3.3.2 for K_{Ic} and $\varepsilon_{\mathrm{EL}}$. The models are then extended in Sec. 3.4 to predict the properties of bcc-based multicomponent alloys and bcc-Ti, bcc-Zr, and bcc-Hf which are unstable at low temperatures.

3.1. Overview of the results with correlation analyses

Fig. 1 summarizes the overall goodness-of-fit R^2 scores for ten properties of τ_{is}, γ_{us}, γ_{s}, Q_{V}, σ_{it}, and γ_{sf} by DFT and H_{B}, σ_{UT}, K_{Ic}, and $\varepsilon_{\mathrm{EL}}$ by experiments from the handbook [58] and the AZoM [59], according to the best (or the second best) individual feature by linear fitting and the combined features selected by the sequential feature selection (SFS) method using the algorithm of support vector machine (SVM) [42]. In addition, Table 2 and Table S 5 list the R^2 scores of the key individual features by linear fitting and the combined features selected by the SVM-based SFS method. Fig. 1 shows that a set of combined features increases the R^2 score from 4 % (for σ_{it}) up to 72 % (for $\varepsilon_{\mathrm{EL}}$) with respect to the individual best feature of each property, demonstrating the capability of data-driven approach to understand and model properties. It can be seen that all DFT-based properties together with experimental H_{B} can be well correlated by individual features with R$^2 > 0.8$ or by the combined features with R$^2 > 0.9$, suggesting that these 7 properties were well predicted or measured with less uncertainties and hence can be

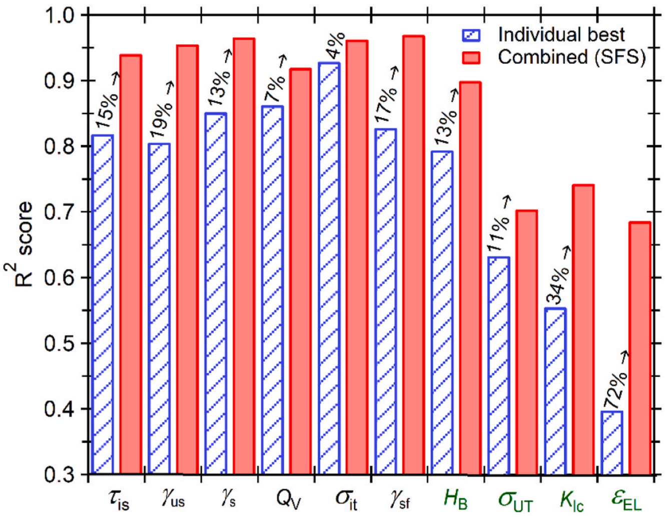

Fig. 1. Overall R^2 scores by correlation analyses for 10 properties of pure elements in terms of (i) the individual best (or the second best) feature and (ii) the combined features suggested by the SFS method, including $\tau_{\rm is}$, $\gamma_{\rm us}$, $\gamma_{\rm s}$, $Q_{\rm V}$, $\sigma_{\rm it}$, and $\gamma_{\rm sf}$ predicted by DFT and $H_{\rm B}$, $\sigma_{\rm UT}$, $K_{\rm Ic}$, and $\varepsilon_{\rm EL}$ by experiments; where the percentages indicate the R^2 improvements.

easily understood and modelled using fundamental materials properties. However, experimental measurements of $\sigma_{\rm UT}$, $K_{\rm Ic}$, and especially $\varepsilon_{\rm EL}$ have low R^2 scores (cf., Fig. 1 and Tables 2 and i.e., $R^2 = 0.62$ for $\sigma_{\rm UT}$, $R^2 = 0.56$ for $K_{\rm Ic}$, and $R^2 = 0.36$ for $\varepsilon_{\rm EL}$) by means of the individual best features; and $R^2 < 0.74$ by the combined features, indicating large variations in these measurements due to stochastic behavior or differences in such as purity, orientation, and grain size, and challenges to understand and model these properties.

As shown in Table 2 and the discussion below, removing data outliers by machine learning based method [42] could greatly increase the predictions for all properties as indicated by the increased R^2 score and the decreased mean absolute error (MAE).

3.2. *Fundamental materials properties by DFT-based calculations*

3.2.1. *ISS (τ_{is}) and USFE (γ_{us})*

A typical DFT-based calculation of fault energy and stress as a function of engineering strain during the pure alias shear deformations is shown in Fig. 2 for hcp Ti on the slip systems of $\{0001\}\langle 10\bar{1}0\rangle$ and $\{10\bar{1}0\}\langle 11\bar{2}0\rangle$. The maximal values correspond to $\gamma_{\rm us}$ (Fig. 2a) and $\tau_{\rm is}$ (Fig. 2b), and both values are lower on the $\{10\bar{1}0\}\langle 11\bar{2}0\rangle$ slip system (0.21 vs. 0.41 J/m^2 for $\gamma_{\rm us}$ and 3.13 vs. 4.39 GPa for $\tau_{\rm is}$) and are selected for the analysis of properties of hcp Ti. It should be mentioned that the determination of $\gamma_{\rm us}$ (under the condition of zero shear stress) is more time-consuming than the determination of $\tau_{\rm is}$ since it is not easy to find an engineering strain with zero shear stress especially for the cases with a sudden jump of stress around $\gamma_{\rm us}$ such as the shear on $\{0001\}\langle 10\bar{1}0\rangle$ for hcp Ti.

Two more examples regarding DFT-based pure alias shear deformations are shown in Figure S 1 for bcc Cr with the antiferromagnetic (AFM) structure on the slip system of $\{1\bar{1}0\}\langle 111\rangle$ to obtain $\gamma_{\rm us}$ and $\tau_{\rm is}$, and in Figure S 2 for fcc Pt on the slip system of $\{111\}\langle 11\bar{2}\rangle$ to obtain $\gamma_{\rm sf}$, $\gamma_{\rm us}$, and $\tau_{\rm is}$. After the pure and even simple shear deformation with relaxations, fcc Pt is the only outlier in the present work with its $\gamma_{\rm us} < \gamma_{\rm sf}$ (0.10 vs. 0.27 J/m^2) using the zero shear stress criterion or $\gamma_{\rm uf} \approx \gamma_{\rm sf}$ (0.29 vs. 0.27 J/m^2) using the $\gamma_{\rm uf} > \gamma_{\rm sf}$ criterion (the present choice).

Table 2

Correlation analyses for the properties of pure elements including $\tau_{\rm is}$, $\gamma_{\rm us}$, $\gamma_{\rm s}$, $Q_{\rm V}$, $\tau_{\rm it}$, and $\gamma_{\rm sf}$ by DFT and $H_{\rm B}$, $\sigma_{\rm UT}$, $K_{\rm Ic}$, and $\varepsilon_{\rm EL}$ by experiments.

Properties	Outliers (>10 %)[a]	Outliers (>3 %)[a]	MAE[b]	R^2 score[b]	Best feature[c]
$\tau_{\rm is}$	bcc Cr, fcc Be	bcc W, hcp Ge, hcp Ce	0.661 ± 0.080 (0.534 ± 0.042)	0.941 ± 0.026 (0.973 ± 0.009)	DFTGh (0.819)
$\gamma_{\rm us}$	hcp Fe, hcp Be	bcc Hg, bcc Cr, fcc Ir	0.035 ± 0.003 (0.029 ± 0.003)	0.956 ± 0.015 (0.973 ± 0.014)	ISS0 (0.806)
$\gamma_{\rm s}$	bcc Cr, hcp Si	fcc Ru, hcp Os, bcc W	0.112 ± 0.009 (0.098 ± 0.008)	0.966 ± 0.007 (0.976 ± 0.006)	EleDensity_Md (0.852)
$Q_{\rm V}$	bcc Cr, hcp Be, hcp Si, fcc Be	hcp Ge, fcc Fe	0.225 ± 0.034 (0.195 ± 0.016)	0.920 ± 0.072 (0.962 ± 0.010)	MeltingT (0.863)
$\tau_{\rm it}$	fcc Mn, fcc Ce	fcc Fe	1.940 ± 0.219 (1.528 ± 0.176)	0.963 ± 0.012 (0.982 ± 0.006)	KIC (0.929)
$\gamma_{\rm sf}$	fcc Fe, fcc Be	fcc Mn, fcc Yb	0.023 ± 0.002 (0.020 ± 0.003)	0.970 ± 0.008 (0.975 ± 0.008)	PBEdiff (0.828)
$H_{\rm B}$	hcp Hf, fcc Ir	bcc W, bcc Cr, hcp Os, hcp Be, fcc Pd	168.8 ± 17.3 (149.6 ± 16.6)	0.900 ± 0.026 (0.929 ± 0.022)	VaQ (0.792)
$\sigma_{\rm UT}$	hcp Co, bcc Cr	bcc Mo	56.53 ± 5.05 (45.68 ± 3.31)	0.704 ± 0.056 (0.846 ± 0.020)	SQGusfp (0.624)
$K_{\rm Ic}$	bcc Mo, hcp Ti, hcp Hf	hcp Be	14.62 ± 1.33 (10.48 ± 1.40)	0.743 ± 0.035 (0.909 ± 0.040)	Surf (0.555)
$\varepsilon_{\rm EL}$	bcc Ta, hcp Cd	fcc Pb	7.97 ± 0.70 (6.60 ± 0.71)	0.686 ± 0.055 (0.782 ± 0.064)	DFTpoisson (0.362)

[a] The outliers (in decreasing importance for the listed elements) are sorted by the frequency of appearance for pure elements with the higher (est) MAE values after 1000 times of SVM trainings using the 5-fold CV method.

[b] The values after the symbol "±" are the standard deviations after 1000 times of SVM trainings using the 5-fold CV method. The values in the parentheses are the results by removing the major outliers (>10 %). The units for the MAE values are GPa for $\tau_{\rm is}$ and $\tau_{\rm it}$; J/m^2 for $\gamma_{\rm sf}$, $\gamma_{\rm us}$, and $\gamma_{\rm s}$, eV for $Q_{\rm V}$, MPa for H_B and $\sigma_{\rm US}$, MPa.m$^{1/2}$ for $K_{\rm Ic}$, and % for $\varepsilon_{\rm EL}$.

[c] The values in the parentheses are the highest (or the second highest) R^2 scores for the selected features according to the filter method of linear fitting. These best features have been used to plot Fig. 1 with more details given in Table S 5.

Fig. 3 summarizes the present (lower) $\tau_{\rm is}$ values for the stable and metastable elements in bcc, fcc, hcp, and/or diamond structures. The present $\tau_{\rm is}$ (and $\gamma_{\rm us}$) values generally agree with the other DFT predictions and experimental measurements at nanoscale in the literature though the data in the literature are scattered due to different methods and different experimental conditions used as shown in Figure S 3 with the values listed in Table S 3 and Table S 4. Figure S 3 indicates the capacity of the pure alias shear deformation to predict properties and gain insights into underlying physics as discussed in Sec. 2.1. Except for the hardest material known today, i.e., carbon diamond with $\tau_{\rm is} = 80$ GPa (the measured result is 75 GPa [60], cf., Table S 3), Fig. 3 shows that the higher $\tau_{\rm is}$ values are for transition metals in the center of the periodic table, such as 20 GPa for fcc Os and 21 GPa for hcp Os followed by 16.9

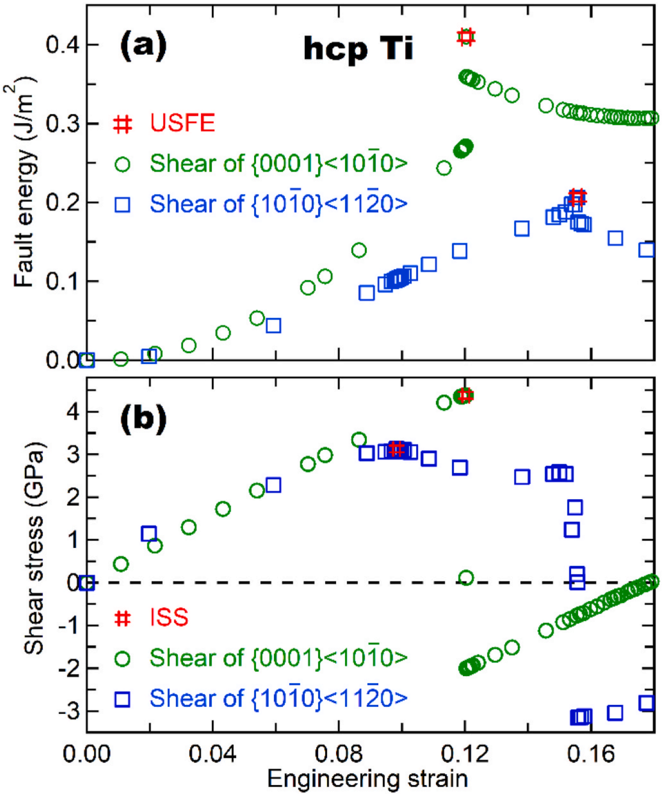

Fig. 2. Pure alias shear deformations of hcp Ti on the slip systems of $\{0001\}\langle 10\bar{1}0\rangle$ and $\{10\bar{1}0\}\langle 11\bar{2}0\rangle$ to predict (a) fault energy and (b) shear stress as a function of engineering strain. The red symbols # indicates the predicted ISS (τ_{is}) and USFE (γ_{us}). (For interpretation of the references to color in this figure legend, the reader is referred to the Web version of this article.)

GPa for bcc Cr and 16.8 GPa for bcc W. The lower τ_{is} values are for alkali metals, alkaline earth metals (except for Be), and some noncentral elements on the periodic table (e.g., Cd, Hg, Tl, Pb, and some lanthanides). Attention should be paid to the outlier element Yb, which is the first element on the periodic table to have the first four shells filled fully and is also the only rare-earth metal which does not follow the trends of the other lanthanides for most properties such as τ_{is}, γ_{us}, γ_s, Q_V, σ_{it}, γ_{sf}, BoilingT, MeltingT, Heat_Fusion, Heat_Sublimation, CohEnergy, DebyeT, Therm_Conduc, and Ele_Conduc (cf., the supplementary Excel file on sheet of All-Data).

Fig. 3 further indicates that the τ_{is} values for elements with the hcp structure are in general higher than those with the fcc structure, except the rare earth elements La to Tb and some central transition metals of Ni, Co, Rh, Ir, Tc, and Re. Ancillary DFT calculations using the same supercell size (i.e., the 6-layer, 24-atom cell) support this conclusion by examining 9 elements of Ir and Rh (larger τ_{is} in fcc structure), and Y, Zr, Ti, Hf, Re, Ru, and Os (larger in hcp); see Figure S 4. In addition, ancillary DFT calculations also indicate that the τ_{is} values are similar ($<$0.5 GPa or $<$ 10 %) on the slip systems of $\{1\bar{1}0\}\langle 111\rangle$, $\{11\bar{2}\}\langle 111\rangle$, and $\{12\bar{3}\}\langle 111\rangle$ (see the supercells used in Table S 6) for Nb and Ta, and especially for Mo and W in the bcc structure. The present results (see supplementary Excel file) agree with the observations in the literature [61,62].

Correlation analyses using linear fitting of individual features indicate that τ_{is} is primarily related to various shear moduli (e.g., DFTGh with $R^2 = 0.819$ and Gvoigt with $R^2 = 0.801$, see Table S 5), as suggested by Frenkel [4] in 1926 and shown by the model #1 in Table 1 (i.e., the feature Gb2pih with $R^2 = 0.783$). Here, Gvoigt is a shear modulus in Voigt approach on the slip systems used in the present work with details in Table S 2 [63,64]. Fig. 4 shows the correlation analyses of τ_{is} versus Gvoigt for each structure. After removing bcc Be, bcc Cr, and fcc Os as the major outliers, the linear fittings show that $\tau_{is}(\text{bcc}) = 0.114G_{\text{Voigt}}(\text{bcc})$ with $R^2 = 0.99$, $\tau_{is}(\text{fcc}) = 0.072G_{\text{Voigt}}(\text{fcc})$ with $R^2 = 0.98$, and $\tau_{is}(\text{hcp}) = 0.068G_{\text{Voigt}}(\text{hcp})$ with $R^2 = 0.93$, illustrating the well correlated relationship between τ_{is} and G by grouping the materials according to their crystal structures. The present τ_{is} vs. G relationships

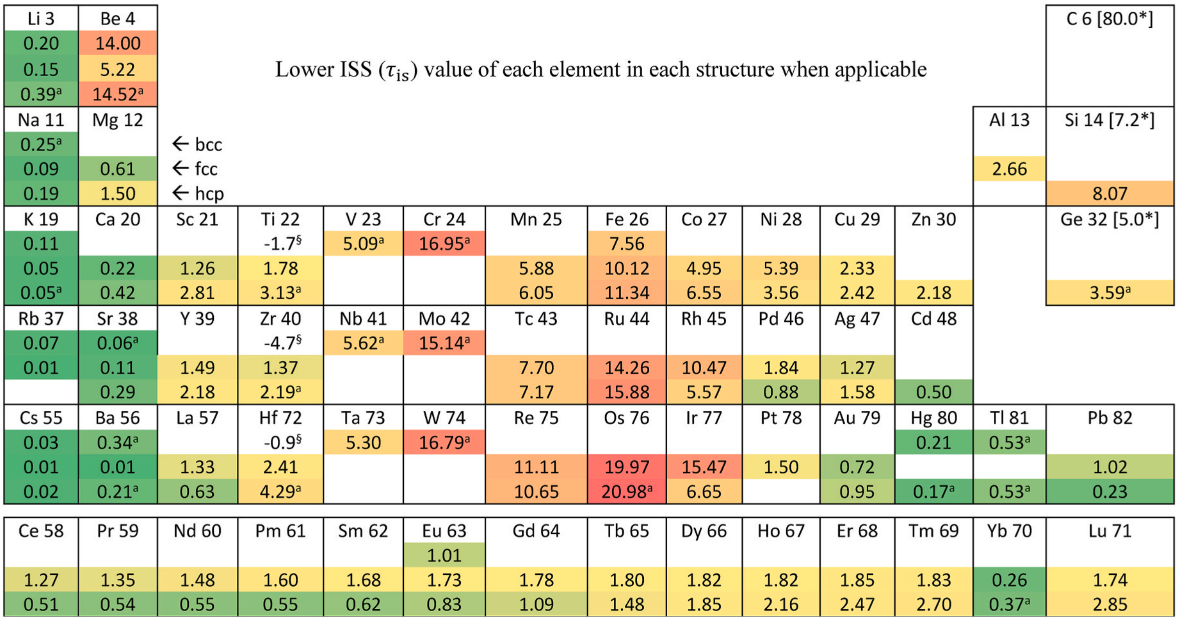

Lower ISS (τ_{is}) value of each element in each structure when applicable

	bcc	fcc	hcp
Li 3	0.20	0.15	0.39^a
Be 4	14.00	5.22	14.52^a
C 6 [80.0*]			
Na 11	0.25^a	0.09	0.19
Mg 12		0.61	1.50
Al 13		2.66	
Si 14 [7.2*]			8.07
K 19	0.11	0.05	0.05^a
Ca 20		0.22	0.42
Sc 21		1.26	2.81
Ti 22	-1.7§	1.78	3.13^a
V 23	5.09^a		
Cr 24	16.95^a		
Mn 25		5.88	6.05
Fe 26	7.56	10.12	11.34
Co 27		4.95	6.55
Ni 28		5.39	3.56
Cu 29		2.33	2.42
Zn 30			2.18
Ge 32 [5.0*]			3.59^a
Rb 37	0.07	0.01	
Sr 38	0.06^a	0.11	0.29
Y 39		1.49	2.18
Zr 40	-4.7§	1.37	2.19^a
Nb 41	5.62^a		
Mo 42	15.14^a		
Tc 43		7.70	7.17
Ru 44		14.26	15.88
Rh 45		10.47	5.57
Pd 46		1.84	0.88
Ag 47		1.27	1.58
Cd 48			0.50
Cs 55	0.03	0.01	0.02
Ba 56	0.34^a	0.01	0.21^a
La 57		1.33	0.63
Hf 72	-0.9§	2.41	4.29^a
Ta 73	5.30		
W 74	16.79^a		
Re 75		11.11	10.65
Os 76		19.97	20.98^a
Ir 77		15.47	6.65
Pt 78		1.50	
Au 79		0.72	0.95
Hg 80	0.21		0.17^a
Tl 81	0.53^a		0.53^a
Pb 82		1.02	0.23
Ce 58		1.27	0.51
Pr 59		1.35	0.54
Nd 60		1.48	0.55
Pm 61		1.60	0.55
Sm 62		1.68	0.62
Eu 63	1.01	1.73	0.83
Gd 64		1.78	1.09
Tb 65		1.80	1.48
Dy 66		1.82	1.85
Ho 67		1.82	2.16
Er 68		1.85	2.47
Tm 69		1.83	2.70
Yb 70		0.26	0.37^a
Lu 71		1.74	2.85

Fig. 3. The present DFT results of ISS (τ_{is} in GPa) for each element in bcc, fcc, hcp, and/or diamond structure (marked by * for C, Si, and Ge). Here, the green (low) – yellow (middle) – red (high) scheme is used to color the data (except for C, Si, and Ge in diamond structure); and the empty places indicate the unstable structures. The superscript a indicates the values in the second slip system (cf., bcc 2 and hcp 2 in Table S 6) are lower than the first one (i.e., bcc 1 and hcp 1), and the values for Ti, Zr, and Hf in bcc structure (marked by §) are estimated by fittings shown in Fig. 14. (For interpretation of the references to color in this figure legend, the reader is referred to the Web version of this article.)

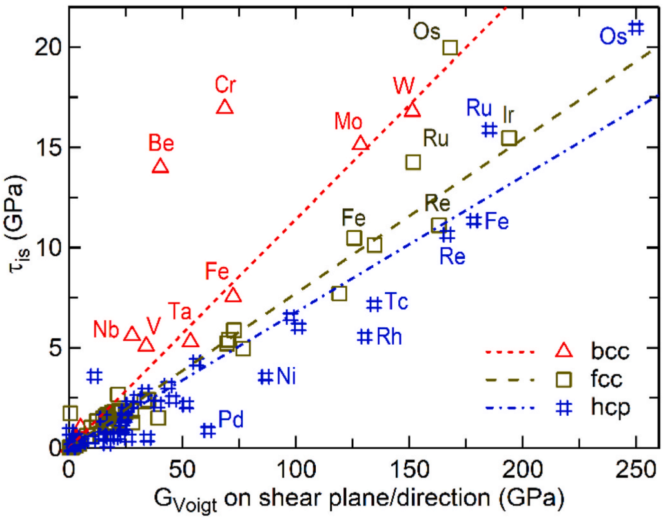

Fig. 4. Correlation analyses via linear fitting for τ_{is} (ISS) vs. shear modulus G_{Voigt} (see Table S 2) for pure elements: $\tau_{is}(bcc) = 0.114G_{Voigt}(bcc)$ with $R^2 = 0.99$ (removing outliers Be and Cr); $\tau_{is}(fcc) = 0.072G_{Voigt}(fcc)$ with $R^2 = 0.98$ (removing Os); and $\tau_{is}(hcp) = 0.068G_{Voigt}(hcp)$ with $R^2 = 0.93$.

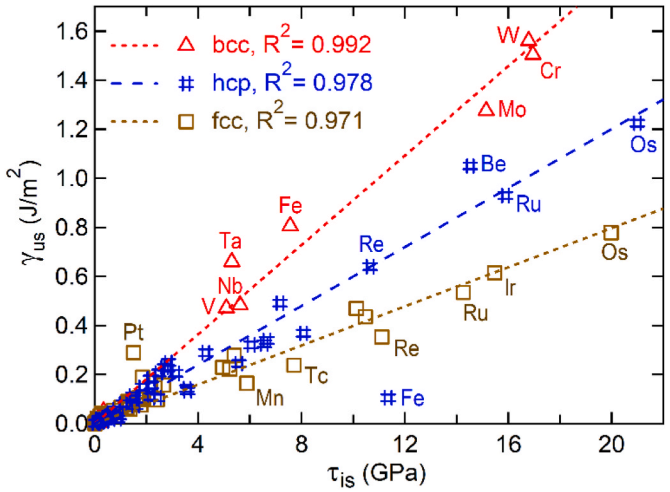

Fig. 6. Correlation analyses of τ_{is} (ISS) vs. γ_{us} (USFE) with the symbols by the present predictions and the lines of linear fittings (by removing hcp Fe and fcc Pt): $\tau_{is}(bcc) = 0.091\gamma_{us}(bcc)$, $\tau_{is}(hcp) = 0.060\gamma_{us}(hcp)$, and $\tau_{is}(fcc) = 0.040\gamma_{us}(fcc)$.

also agree quantitatively with the suggestions in the literature, for example, $\tau_{is}(bcc) = 0.11G(bcc)$ and $\tau_{is}(fcc) = 0.08G(fcc)$ [62,65]. In addition to shear modulus, Q_V is another key parameter related to τ_{is} according to the SVM-based SFS method as shown in Table S 5. By removing the outliers with their frequency of appearances $f_{out} > 10\%$ during 1000 times of trainings using the 5-fold cross validation method, the R^2 score increases from 0.941 to 0.973, and the MAE values decrease from 0.661 to 0.534 GPa in predicting τ_{is} using the combined features in Table 2, indicating the capability of these features to sort outliers and predict τ_{is}.

Fig. 5 summarizes the present (lower) γ_{us} values for elements in stable and metastable bcc, fcc, hcp, and/or diamond structures. These γ_{us} values follow similar trends as those of τ_{is}, except the larger γ_{us} values being for W, Mo, and Cr in the bcc structure. Correlation analyses using linear fitting indicate that γ_{us} correlates to τ_{is} with $R^2 = 0.806$, while the other features have less correlations with $R^2 < 0.6$ as shown in Table S 5. A further examination as shown in Fig. 6 indicates that $\tau_{is}(bcc) = 0.091\gamma_{us}(bcc)$ with $R^2 = 0.992$, $\tau_{is}(hcp) = 0.060\gamma_{us}(hcp)$ with $R^2 = 0.978$ after removing the outlier of hcp Fe, and $\tau_{is}(fcc) = 0.040\gamma_{us}(fcc)$ with $R^2 = 0.971$ after removing the outlier of fcc Pt. These high R^2 scores suggest that we can ignore the time-consuming DFT calculations to find γ_{us}, and alternatively, we can model γ_{us} by τ_{is}, supporting the suggestion by Rice [13] as shown by the model #2 in Table 1.

Like the τ_{is} case, using the combined features by the SVM-based SFS method and removing the major outliers with $f_{out} > 10\%$ increase the R^2 score (from 0.956 to 0.973) and decrease the MEA values (from 0.035 to 0.029 J/m^2) as shown in Table 2.

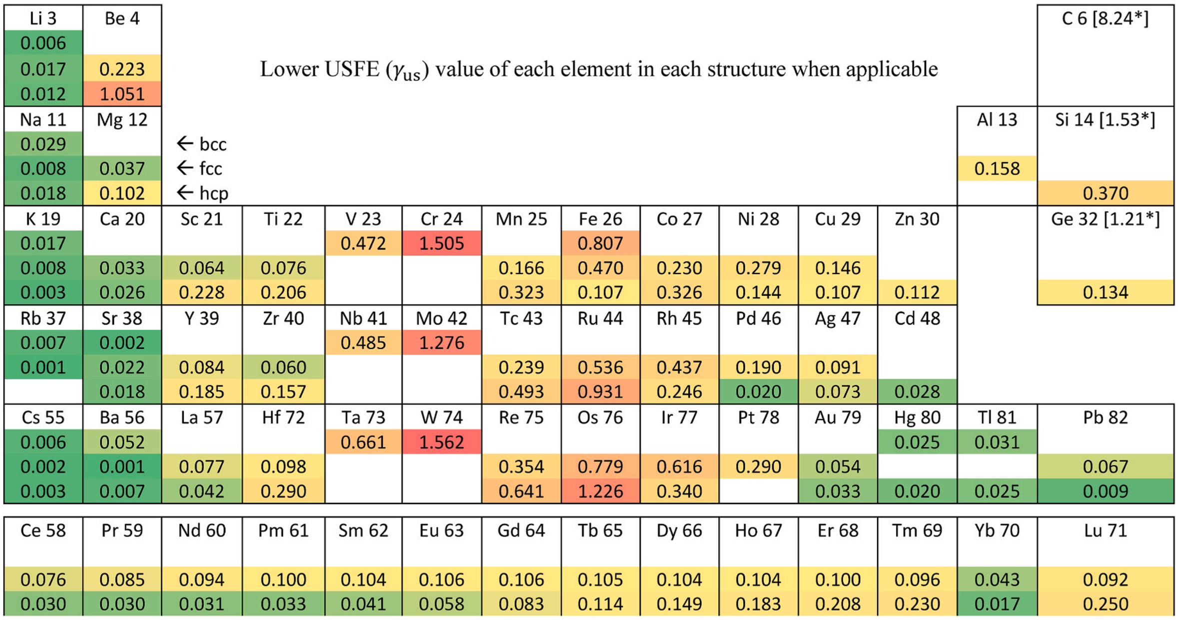
Lower USFE (γ_{us}) value of each element in each structure when applicable

Li 3	Be 4												C 6 [8.24*]
0.006													
0.017	0.223												
0.012	1.051												
Na 11	Mg 12											Al 13	Si 14 [1.53*]
0.029		← bcc											
0.008	0.037	← fcc										0.158	
0.018	0.102	← hcp											0.370
K 19	Ca 20	Sc 21	Ti 22	V 23	Cr 24	Mn 25	Fe 26	Co 27	Ni 28	Cu 29	Zn 30		Ge 32 [1.21*]
0.017				0.472	1.505		0.807						
0.008	0.033	0.064	0.076			0.166	0.470	0.230	0.279	0.146			
0.003	0.026	0.228	0.206			0.323	0.107	0.326	0.144	0.107	0.112		0.134
Rb 37	Sr 38	Y 39	Zr 40	Nb 41	Mo 42	Tc 43	Ru 44	Rh 45	Pd 46	Ag 47	Cd 48		
0.007	0.002			0.485	1.276								
0.001	0.022	0.084	0.060			0.239	0.536	0.437	0.190	0.091			
	0.018	0.185	0.157			0.493	0.931	0.246	0.020	0.073	0.028		
Cs 55	Ba 56	La 57	Hf 72	Ta 73	W 74	Re 75	Os 76	Ir 77	Pt 78	Au 79	Hg 80	Tl 81	Pb 82
0.006	0.052			0.661	1.562						0.025	0.031	
0.002	0.001	0.077	0.098			0.354	0.779	0.616	0.290	0.054			0.067
0.003	0.007	0.042	0.290			0.641	1.226	0.340		0.033	0.020	0.025	0.009

Ce 58	Pr 59	Nd 60	Pm 61	Sm 62	Eu 63	Gd 64	Tb 65	Dy 66	Ho 67	Er 68	Tm 69	Yb 70	Lu 71
0.076	0.085	0.094	0.100	0.104	0.106	0.106	0.105	0.104	0.104	0.100	0.096	0.043	0.092
0.030	0.030	0.031	0.033	0.041	0.058	0.083	0.114	0.149	0.183	0.208	0.230	0.017	0.250

Fig. 5. The present DFT results of USFE (γ_{us} in J/m^2) for each element in bcc, fcc, hcp, and/or diamond structure (values marked by * for C, Si, and Ge). Here, the green (low) – yellow (middle) – red (high) scheme is used to color the data; and the empty places indicate the unstable structures. (For interpretation of the references to color in this figure legend, the reader is referred to the Web version of this article.)

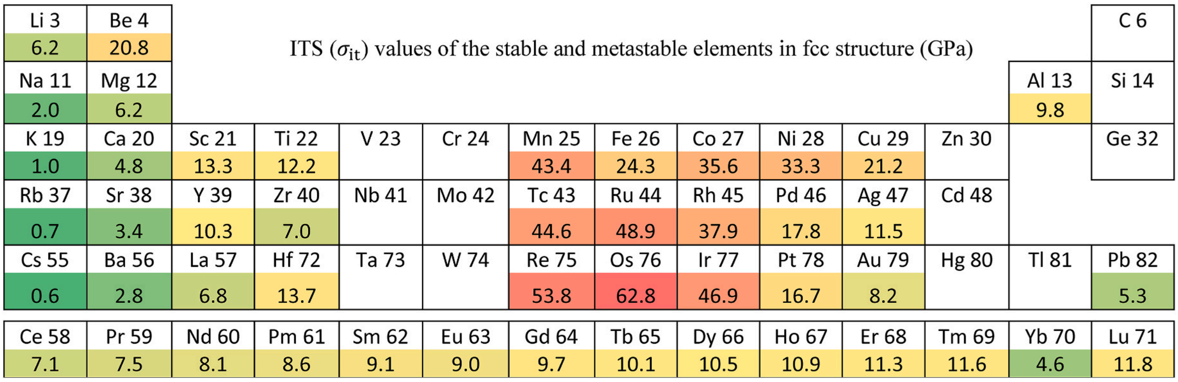

ITS (σ_{it}) values of the stable and metastable elements in fcc structure (GPa)

Li 3 6.2	Be 4 20.8												C 6
Na 11 2.0	Mg 12 6.2											Al 13 9.8	Si 14
K 19 1.0	Ca 20 4.8	Sc 21 13.3	Ti 22 12.2	V 23	Cr 24	Mn 25 43.4	Fe 26 24.3	Co 27 35.6	Ni 28 33.3	Cu 29 21.2	Zn 30		Ge 32
Rb 37 0.7	Sr 38 3.4	Y 39 10.3	Zr 40 7.0	Nb 41	Mo 42	Tc 43 44.6	Ru 44 48.9	Rh 45 37.9	Pd 46 17.8	Ag 47 11.5	Cd 48		
Cs 55 0.6	Ba 56 2.8	La 57 6.8	Hf 72 13.7	Ta 73	W 74	Re 75 53.8	Os 76 62.8	Ir 77 46.9	Pt 78 16.7	Au 79 8.2	Hg 80	Tl 81	Pb 82 5.3
Ce 58 7.1	Pr 59 7.5	Nd 60 8.1	Pm 61 8.6	Sm 62 9.1	Eu 63 9.0	Gd 64 9.7	Tb 65 10.1	Dy 66 10.5	Ho 67 10.9	Er 68 11.3	Tm 69 11.6	Yb 70 4.6	Lu 71 11.8

Fig. 7. The present DFT results of ITS (σ_{it} in GPa) for pure elements in fcc structure via pure tensile deformations along the ⟨111⟩ direction. Here, the green (low) – yellow (middle) – red (high) scheme is used to color the data; and the empty places indicate the unstable fcc structures. (For interpretation of the references to color in this figure legend, the reader is referred to the Web version of this article.)

3.2.2. *Other DFT-based properties*

Fig. 7 summarizes the σ_{it} values of the stable and metastable pure elements in fcc structure predicted by DFT-based pure tensile deformations in the present work. As two examples, Figure S 5 shows the tensile stress vs. tensile strain (represented by the lattice parameters c/a ratio) curves for fcc Al with a sharp drop near σ_{it} and fcc Au with a continuous change near σ_{it}. In general, the present σ_{it} values agree with the other DFT predictions in the literature [1], which are scattered as shown in Figure S 6. Fig. 7 depicts clear trends on the periodic table with the higher σ_{it} being for Os followed by Re and Ru and the lower being for alkali metals. Correlation analysis indicates that σ_{it} connects well with several individual features with $R^2 > 0.8$, for example, C_{11}, C_{33}, and Young's modulus as shown in Table S 5. Figure S 7 also indicates that the σ_{it} values can be modelled well using the empirical model $\sigma_{\text{it}} = \sqrt{E\gamma_{\text{s}}/h}$ with $R^2 = 0.983$, corresponding to the model #4 in Table 1 [14].

Fig. 8 summarizes the γ_{sf} values of the stable and metastable pure elements in the fcc structure predicted by DFT-based pure alias shear deformations in the present work, agreeing well with experimental data in the literature for 9 fcc elements of Ag, Al, Au, Cu, Ir, Ni, Pd, Pt, and Rh [42]. Fig. 8 shows the higher positive γ_{sf} values for Ir and Pt (>270 mJ/m^2) and the lower negative ones for Os, Be, and Ru, which are stable in the hcp structure (<-530 mJ/m^2). Table S 5 shows that the γ_{sf} values only correlate well with the energy difference between the hcp and fcc structures ($\Delta E_{\text{hcp-fcc}}$) with $R^2 = 0.83$ (or 0.9 without the outlier Yb). A further analysis (Figure S 8) indicates that the relationship of γ_{sf} vs. $\Delta E_{\text{hcp-fcc}}$ could achieve $R^2 \approx 1$ by analyzing only the rare-earth elements (without Yb) or only the elements with $\gamma_{\text{sf}} > 0$ (without Yb and La).

Surface energy γ_{s} from the literature is shown in Figure S 9 [26,27] and correlates well with electron density (EleDensity_Md) with $R^2 = 0.852$ as depicted in Figure S 10, Q_{V} with $R^2 = 0.83$, and more features with $R^2 > 0.7$ as shown in Table S 5. Q_{V} from the literature [29] correlates well with melting temperature (MeltingT) with $R^2 = 0.863$ as well as more other features with $R^2 > 0.7$ as shown in Table S 5. Similar to the properties discussed above, the R^2 scores for correlating γ_{s} and Q_{V} can be improved using the combined features and/or removing the outliers as shown in Table 2.

3.3. *Mechanical properties by experiments*

For the measured H_{B}, σ_{UT}, K_{Ic}, and ε_{EL} as collected in the handbook [58] and in the website AZoM [59] for pure elements (see detailed AZoM websites in the supplemental Excel file), correlation analyses show that the H_{B} data are more accurate according to the comparisons between the handbook data and the AZoM data with the R^2 scores by linear fitting being 0.9 for H_{B}, 0.8 for σ_{UT} , and 0.77 for ε_{EL} as shown in Figure S 11, Figure S 12, and Figure S 14, respectively. Note that the K_{Ic} data are not available in the handbook [58]. Based on the minimal and the maximal values collected in AZoM for each property as shown in Figure S 11 to Figure S 14, we conclude that the ε_{EL} data have the largest uncertainty with the average error up to 65 % as shown in Figure S 14, and the second largest uncertainty is for K_{Ic} with the average percentage error up to 54 % as shown in Figure S 13.

3.3.1. *Brinell hardness (H_{B}) and ultimate tensile strength (UT, σ_{UT})*

Table 2 and Table S 5 show that the measured H_{B} values of pure elements can be correlated by several individual features such as Q_{V} with $R^2 = 0.79$ and SQGusfp as #95 in Table S 2 with $R^2 = 0.733$. Fig. 9 plots the H_{B} versus Q_{V} relationship for pure elements in bcc, fcc, or hcp

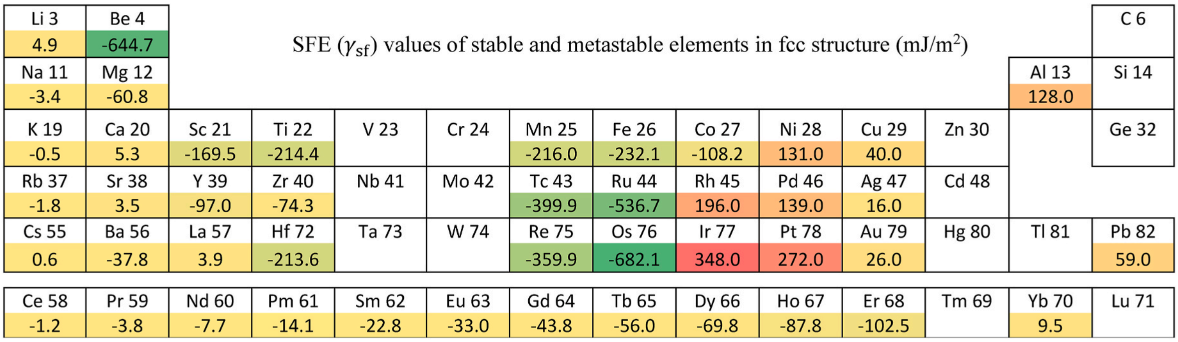

SFE (γ_{sf}) values of stable and metastable elements in fcc structure (mJ/m^2)

Li 3 4.9	Be 4 -644.7												C 6
Na 11 -3.4	Mg 12 -60.8											Al 13 128.0	Si 14
K 19 -0.5	Ca 20 5.3	Sc 21 -169.5	Ti 22 -214.4	V 23	Cr 24	Mn 25 -216.0	Fe 26 -232.1	Co 27 -108.2	Ni 28 131.0	Cu 29 40.0	Zn 30		Ge 32
Rb 37 -1.8	Sr 38 3.5	Y 39 -97.0	Zr 40 -74.3	Nb 41	Mo 42	Tc 43 -399.9	Ru 44 -536.7	Rh 45 196.0	Pd 46 139.0	Ag 47 16.0	Cd 48		
Cs 55 0.6	Ba 56 -37.8	La 57 3.9	Hf 72 -213.6	Ta 73	W 74	Re 75 -359.9	Os 76 -682.1	Ir 77 348.0	Pt 78 272.0	Au 79 26.0	Hg 80	Tl 81	Pb 82 59.0
Ce 58 -1.2	Pr 59 -3.8	Nd 60 -7.7	Pm 61 -14.1	Sm 62 -22.8	Eu 63 -33.0	Gd 64 -43.8	Tb 65 -56.0	Dy 66 -69.8	Ho 67 -87.8	Er 68 -102.5	Tm 69	Yb 70 9.5	Lu 71

Fig. 8. The present DFT results of stable stacking fault energy (SFE or γ_{sf} in mJ/m^2) for elements in fcc structure. Here, the green (low) – yellow (middle) – red (high) scheme is used to color the data; and the empty places indicate the unstable fcc structure. (For interpretation of the references to color in this figure legend, the reader is referred to the Web version of this article.)

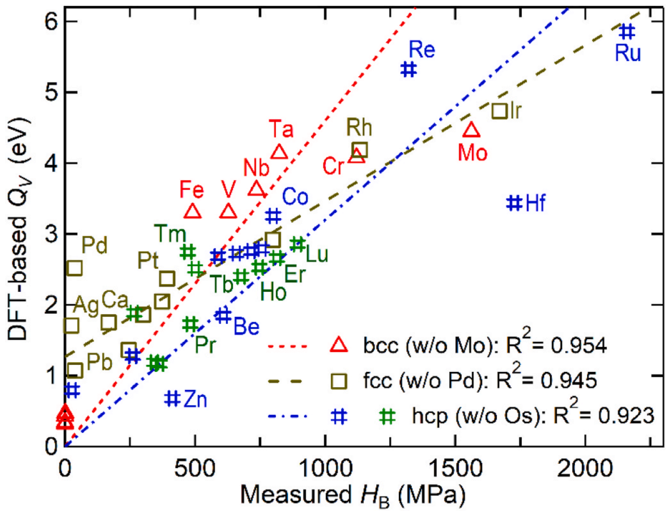

Fig. 9. Relationship between the measured hardness (H_B) and DFT-based vacancy activation energy (Q_V) with the lines being linear fittings.

structures after removing the outliers (bcc Mo, fcc Pd, and hcp Os). The high R^2 scores (>0.92) indicate that H_B can be modelled well by Q_V. Table S 5 shows the combined 8 features listed in Table S 2 to model H_B with $R^2 = 0.9$, indicating the critical role of Q_V, γ_{us}, τ_{is}, shear modulus, electronegativity, and electron density in modeling H_B. The same as the above observations, the R^2 score increases to 0.93 after removing the outliers of hcp Hf and fcc Ir with $f_{out} > 10\%$. The higher R^2 scores (>0.9) in terms of the combined features also imply that the H_B data in the handbook [58] are in high quality.

Table 2 and Table S 5 show that σ_{UT} can be modelled relatively well by using such as SQGusfp with $R^2 = 0.624$. Using the selected 6 features (Heat_Fusion, SQGusfp, normUSFE, Period, SQusf, and Heat_Capacity) by the SVM-based SFS method, the R^2 score for σ_{UT} increases to 0.7 or up to 0.85 by removing the outliers of hcp Co and bcc Cr with $f_{out} > 10\%$ (see Fig. 10). These features suggest that σ_{UT} connects to elastic, plastic, and thermodynamic properties (G, ν, γ_{us}, heat of fusion, and heat capacity), supporting the model #9 in Table 1.

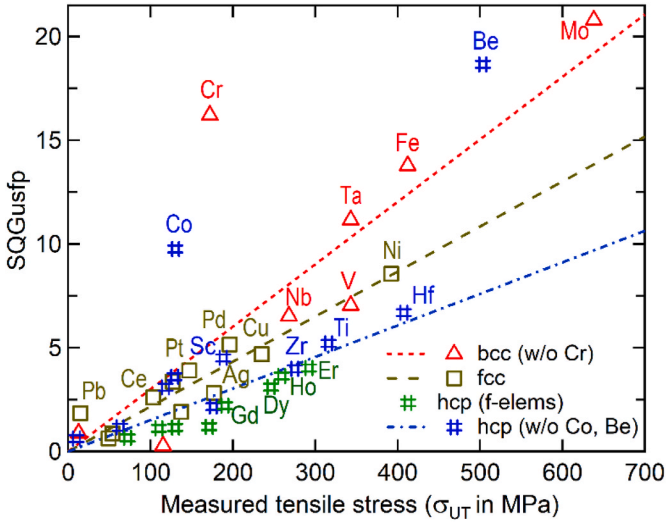

Fig. 10. Measured ultimate tensile stress (σ_{UT} in MPa) versus DFT-based $\sqrt{2G\gamma_{us}/(1-\nu)}$ (i.e., the SQGusfp in Table S 2; see the model #10 in Table 1). The linear fittings result in: $y(\text{bcc}) = 0.0301\ \sigma_{TS}(\text{bcc})$ with $R^2 = 0.966$, $y(\text{fcc}) = 0.0217\ \sigma_{UT}(\text{fcc})$ with $R^2 = 0.961$, and $y(\text{hcp}) = 0.0152\ \sigma_{UT}(\text{hcp})$ with $R^2 = 0.933$; where y = SQGusfp.

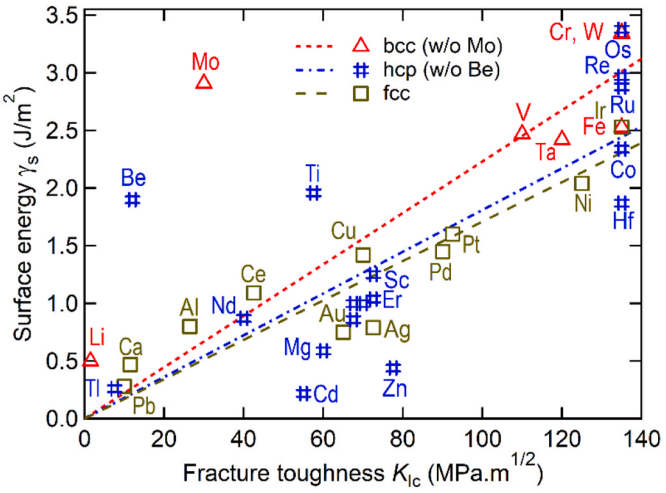

Fig. 11. Measured fracture toughness vs. DFT-based surface energy with the lines being linear fittings: $\gamma_s(\text{bcc}) = 0.0223K_{Ic}(\text{bcc})$ with $R^2 = 0.98$, $\gamma_s(\text{fcc}) = 0.0171K_{Ic}(\text{fcc})$ with $R^2 = 0.96$, and $\gamma_s(\text{hcp}) = 0.0181K_{Ic}(\text{hcp})$ with $R^2 = 0.90$.

3.3.2. *Fracture toughness (FracT, K_{Ic}) and relative elongation (Elong, ε_{EL})*

Table 2 and Table S 5 show that FracT or K_{Ic} can be roughly modelled by using such as γ_s with $R^2 = 0.56$, Q_V with $R^2 = 0.55$, or KGS with $R^2 = 0.49$. Fig. 11 shows the examinations of K_{Ic} vs. γ_s for pure elements in bcc, fcc, or hcp structures with the outliers of bcc Mo and hcp Be removed, promoting $R^2 > 0.9$. In addition, the R^2 score increases to 0.74 or 0.91 using the combined features, including γ_s, NpUnfill, Ion_Pot_3, Radius_Coval, Heat_Capacity, and ratio_bh, after removing the outliers. These results and the R^2 scores support at least the model #11 in Table 1 with γ_s being the key feature to model K_{Ic}.

It is observed that ε_{EL} from experiments [58] cannot correlate to any individual features with $R^2 < 0.4$, for all features as shown in Table S 5 due to the very scattered ε_{EL} data of pure elements in Figure S 14. The low R^2 scores do not support any models in Table 1 (#13 to #19). Using the combined features (Table S 5), the R^2 score increases to 0.69 or 0.78 after removing the outliers. The combined features work better than the individual ones but still not enough to build a predictive model for ε_{EL} due mainly to the poor data quality from experiments [58]. By examining the ε_{EL} values for subsets of elements, one can find some trends between ε_{EL} and the features, such as ε_{EL} vs. the groups of fcc elements

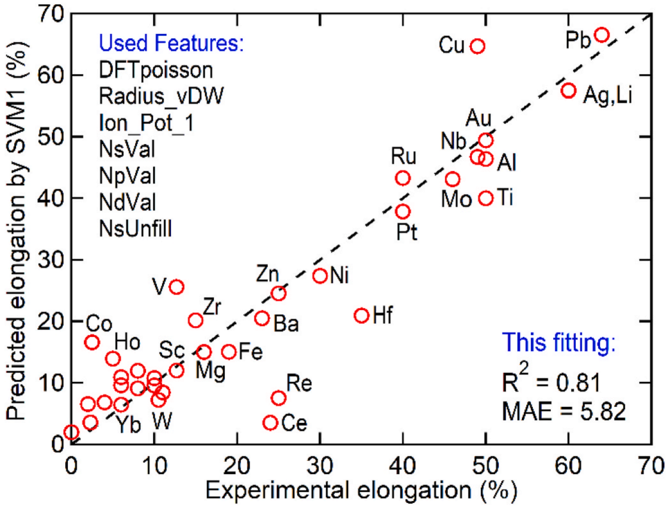

Fig. 12. Predicted relative elongation using SVM1 using the combined features and the 5-fold cross validation method.

with $R^2 = 0.88$ by linear fitting as shown in Figure S 15. In addition, Fig. 12 shows one of the predicted ε_{EL} results in comparison with experimental ε_{EL} data [58] using the SVM1 algorithm in terms of the combined features and the 5-fold cross validation, achieving reasonable predictions with $R^2 = 0.81$ and MEA = 5.85 %.

3.4. *From pure elements to multicomponent phases*

Properties of pure elements are the foundation for understanding and modeling properties of multicomponent phases and even under unstable conditions using the machine learning- or CALPHAD-based approaches as shown by Eq. (1). For example, Figure S 16 shows a very good relationship with $R^2 \approx 1$ in terms of linear fitting of surface energies for bcc-based Ti-Zr-Hf-V-Nb-Ta-Mo-W-Re-Ru alloys between the rule-of-mixture estimations using the γ_s values of pure elements (i.e., $\phi_0 = \sum_i x_i \phi_{0,i}$ in Eq. (1)) and the DFT-based predictions using the binary, ternary, and quaternary SQS's [66].

Fig. 13 depicts that the modelled τ_{is} values for 10 bcc-based binary alloys in the Mo-Nb-Ta-V-W system by using the one- or two-parameter R-K polynormal [23], in addition to the $\phi_{0,i}$ values for pure elements in Eq. (1). For each binary alloy such as Mo-Ta, the R-K fitting was performed with five DFT data points calculated on the slip system $\{11\bar{2}\}\langle 111\rangle$ using the 24-atom supercells as shown in Table S 6, i.e., the configurations of Mo_{24}, $Mo_{23}Ta$ for the dilute solution with one Ta on the slip plane, $Mo_{12}Ta_{12}$ concentrated solution using SQS's, $MoTa_{23}$ for the dilute solution, and Ta_{24}. The resulted τ_{is} values are presented in the supplementary Excel file. The modelled parameters $\phi_{0,i}$ and $\phi_{ij}^{(L)}$ indicate that the τ_{is} values can be modelled in the whole Mo-Nb-Ta-V-W system according to the general CALPHAD modeling approach of Eq. (1) as depicted in Fig. 13.

Fig. 13 shows that the fittings for the Mo-X (X = Nb, Ta, V, and W) alloys are with smaller fitting errors in comparation with the other fittings. The bcc-based Mo-Ti, Mo-Zr, and Mo-Hf systems are hence selected to evaluate the τ_{is} values of bcc-Ti, bcc-Zr, and bcc-Hf which are unstable at low temperatures with one R-K parameter as shown in Fig. 14. It is observed that the τ_{is} values for bcc-Ti, bcc-Zr, and bcc-Hf are negative, i.e., being unstable in agreement with the conclusions using the matrices of elastic constants [25]. Fig. 14 also depicts that Ti, Zr, and Hf follow the similar trends with the highest τ_{is} being for Hf, then Ti and Zr in each of the hcp, fcc, and bcc structures.

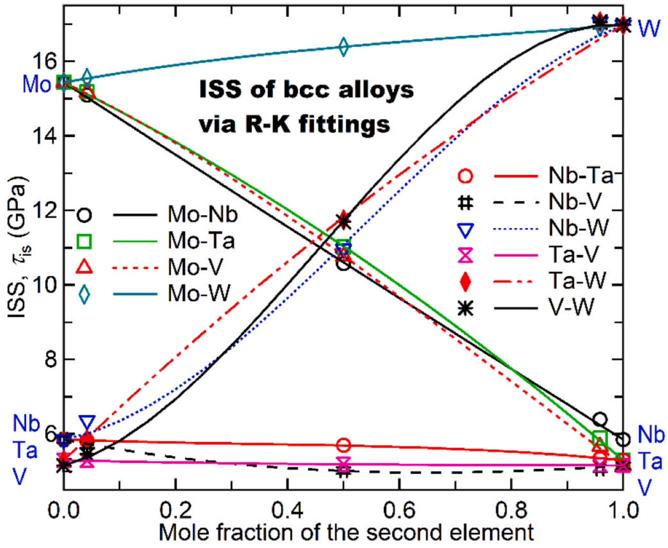

Fig. 13. ISS (τ_{is}) values of bcc-based binary alloys by CALPHAD-based Redlich-Kistler (R–K) fittings, where the symbols are DFT-based results of pure elements, dilute alloys, and concentrated alloys (using SQS's).

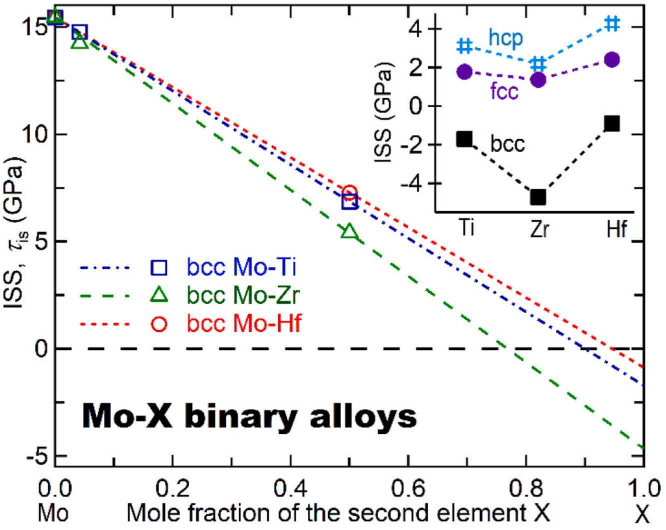

Fig. 14. ISS (τ_{is}) values of bcc-based Mo-X (X = Ti, Zr, and Hf) alloys with the symbols being DFT-based results and the lines being linear fittings to estimate τ_{is} values of the unstable Ti, Zr, and Hf in bcc structure. The inset shows the τ_{is} values of Ti, Zr, and Hf in fcc, hcp, and bcc structures.

The plots in Figure S 16, Figs. 13, and Fig. 14 suggest that the general CALPHAD modeling approach [21,22] is able to model properties of phases under stable, metastable, and unstable conditions in multicomponent systems starting from materials properties of pure elements as shown by Eq. (1).

4. Summary

The present work provides digital data of fundamental properties for 60 pure elements in bcc, fcc, hcp, and/or diamond structures from the literature and the present DFT calculations using the pure alias shear and the pure tensile deformations. The present data compilation enables data-driven insights into pure elements, for example, the 10 properties of pure elements as examined in the present work: τ_{is}, γ_{us}, γ_s, Q_V, σ_{it}, and γ_{sf} predicted by DFT and H_B, σ_{UT}, K_{Ic}, and ε_{EL} from experiments. Correlation analyses suggest new and existing features and models to predict mechanical properties. For example, ideal shear strength τ_{is} is highly correlated to G, γ_{us} to τ_{is}, H_B to Q_V, σ_{UT} to $\sqrt{\gamma_s}$ or $\sqrt{\gamma_{us}}$, and K_{Ic} to γ_s. However, no satisfactory models are found to correlate ε_{EL} due to high uncertainty of datasets, and the empirical models listed in Table 1 are only validated for a certain range of elements/materials based on the present correlation analyses. Data-enabled analyses also identify the outliers of pure elements, e.g., Cr in τ_{is}, γ_s, Q_V, and σ_{UT}, Be in τ_{is}, γ_{sf}, γ_{us}, and Q_V, Hf in H_B and K_{Ic}, Yb in all properties, and Pt in γ_{sf} vs. γ_{us}. Starting from digital data of pure elements, the present data compilation enables the prediction of properties of multicomponent phases even under unstable conditions, as demonstrated for γ_s and τ_{is} in bcc-based alloys and τ_{is} for Ti, Zr, and Hf in the bcc structure in terms of the general CALPHAD modeling approach.

CRediT authorship contribution statement

Shun-Li Shang: Writing – review & editing, Writing – original draft, Methodology, Investigation, Formal analysis, Data curation. **Michael C. Gao:** Writing – review & editing, Supervision, Conceptualization. **Yi Wang:** Writing – review & editing, Methodology. **Jingjing Li:** Writing – review & editing, Supervision, Funding acquisition, Conceptualization. **Allison M. Beese:** Writing – review & editing, Supervision, Funding acquisition, Conceptualization. **Zi-Kui Liu:** Writing – review & editing, Supervision, Methodology, Funding acquisition, Conceptualization.

Declaration of competing interest

The authors declare that they have no known competing financial interests or personal relationships that could have appeared to influence the work reported in this paper.

Acknowledgements

This work was primarily funded by the U.S. Department of Energy (DOE) through Grant No. DE-AR0001435; partially supported by the National Science Foundation (NSF) via Award Nos. CMMI-2050069 (A. M. Beese) and CMMI-2226976 (J. J. Li), and by the Office of Naval Research (ONR) via Contract No.: N00014-21-1-2608 (A. M. Beese); and partially supported by the DOE eXtermeMAT (XMAT) project and the DOE High Performance Computing for Energy Innovation (HPC4EI) on the project “Accelerating High Temperature Operation Development of High Entropy Alloys via High Performance Computation”, and through an appointment to DOE Faculty Research Program at the National Energy Technology Laboratory (NETL) administered by the Oak Ridge Institute for Science and Education (S. L. Shang). First-principles calculations were performed partially on the Roar supercomputers at the Pennsylvania State University’s Institute for Computational and Data Sciences (ICDS), partially on the resources of the National Energy Research Scientific Computing Center (NERSC) supported by the DOE Office of Science User Facility operated under Contract no. DE-AC02-05CH11231 using NERSC Award No. ALCC-ERCAP0022624, and partially on the resources of the Extreme Science and Engineering Discovery Environment (XSEDE) supported by NSF with Grant no. ACI-1548562.

Appendix A. Supplementary data

Supplementary data to this article can be found online at https://doi.org/10.1016/j.msea.2024.147446.

Data availability

Data will be made available on request.

References

[1] J. Pokluda, M. Černý, M. Šob, Y. Umeno, Ab initio calculations of mechanical properties: methods and applications, Prog. Mater. Sci. 73 (2015) 127–158, https://doi.org/10.1016/j.pmatsci.2015.04.001.

[2] E.P. George, W.A. Curtin, C.C. Tasan, High entropy alloys: a focused review of mechanical properties and deformation mechanisms, Acta Mater. 188 (2020) 435–474, https://doi.org/10.1016/j.actamat.2019.12.015.

[3] J.J. Lewandowski, M. Seifi, Metal additive manufacturing: a review of mechanical properties, Annu. Rev. Mater. Res. 46 (2016) 151–186, https://doi.org/10.1146/annurev-matsci-070115-032024.

[4] J. Frenkel, Zur Theorie der Elastizitätsgrenze und der Festigkeit kristallinischer Körper, Z. Phys. 37 (1926) 572–609, https://doi.org/10.1007/BF01397292.

[5] H. Niu, S. Niu, A.R. Oganov, Simple and accurate model of fracture toughness of solids, J. Appl. Phys. 125 (2019) 065105, https://doi.org/10.1063/1.5066311.

[6] S.F. Pugh, XCII. Relations between the elastic moduli and the plastic properties of polycrystalline pure metals, Philos. Mag. A 45 (1954) 823–843, https://doi.org/10.1080/14786440808520496.

[7] A. Kelly, W.R. Tyson, A.H. Cottrell, Ductile and brittle crystals, Philos. Mag. A J. Theor. Exp. Appl. Phys. 15 (1967) 567–586, https://doi.org/10.1080/14786436708220903.

[8] S. Ogata, J. Li, Toughness scale from first principles, J. Appl. Phys. 106 (2009) 113534, https://doi.org/10.1063/1.3267158.

[9] J.R. Rice, R. Thomson, Ductile versus brittle behaviour of crystals, Philos. Mag. A J. Theor. Exp. Appl. Phys. 29 (1974) 73–97, https://doi.org/10.1080/14786437408213555.

[10] S. Kamran, K. Chen, L. Chen, *Ab initio* examination of ductility features of fcc metals, Phys. Rev. B 79 (2009) 024106, https://doi.org/10.1103/PhysRevB.79.024106.

[11] K. Balasubramanian, S.V. Khare, D. Gall, Valence electron concentration as an indicator for mechanical properties in rocksalt structure nitrides, carbides and carbonitrides, Acta Mater. 152 (2018) 175–185, https://doi.org/10.1016/j.actamat.2018.04.033.

[12] G. Hua, D. Li, Electron work function: a novel probe for toughness, Phys. Chem. Chem. Phys. 18 (2016) 4753–4759, https://doi.org/10.1039/C5CP04873G.

[13] J.R. Rice, Dislocation nucleation from a crack tip: an analysis based on the Peierls concept, J. Mech. Phys. Solid. 40 (1992) 239–271, https://doi.org/10.1016/S0022-5096(05)80012-2.

[14] N.H. Macmillan, A. Kelly, On the relationship between ideal tensile strength and surface energy, Mater. Sci. Eng. 10 (1972) 139–143, https://doi.org/10.1016/0025-5416(72)90078-X.

[15] B. Joós, M.S. Duesbery, The Peierls stress of dislocations: an analytic formula, Phys. Rev. Lett. 78 (1997) 266–269, https://doi.org/10.1103/PhysRevLett.78.266.

[16] M. Jo, Y.M. Koo, B.-J. Lee, B. Johansson, L. Vitos, S.K. Kwon, Theory for plasticity of face-centered cubic metals, Proc. Natl. Acad. Sci. USA 111 (2014) 6560–6565, https://doi.org/10.1073/PNAS.1400786111.

[17] R.J. Asaro, S. Suresh, Mechanistic models for the activation volume and rate sensitivity in metals with nanocrystalline grains and nano-scale twins, Acta Mater. 53 (2005) 3369–3382, https://doi.org/10.1016/J.ACTAMAT.2005.03.047.

[18] X.-Q. Chen, H. Niu, D. Li, Y. Li, Modeling hardness of polycrystalline materials and bulk metallic glasses, Intermetallics 19 (2011) 1275–1281, https://doi.org/10.1016/j.intermet.2011.03.026.

[19] C. Deng, F. Sansoz, Fundamental differences in the plasticity of periodically twinned nanowires in Au, Ag, Al, Cu, Pb and Ni, Acta Mater. 57 (2009) 6090–6101, https://doi.org/10.1016/j.actamat.2009.08.035.

[20] R.M. Thomson, Physics of fracture, J. Phys. Chem. Solid. 48 (1987) 965–983, https://doi.org/10.1016/0022-3697(87)90114-4.

[21] S. Shang, Y. Wang, Y. Du, M.A. Tschopp, Z.-K. Liu, Integrating computational modeling and first-principles calculations to predict stacking fault energy of dilute multicomponent Ni-base alloys, Comput. Mater. Sci. 91 (2014) 50–55, https://doi.org/10.1016/j.commatsci.2014.04.040.

[22] H.L. Lukas, S.G. Fries, B. Sundman, Computational Thermodynamics: the CALPHAD Method, Cambridge University Press, 2007.

[23] O. Redlich, A.T. Kister, Algebraic representation of thermodynamic properties and the classification of solutions, Ind. Eng. Chem. 40 (1948) 345–348, https://doi.org/10.1021/ie50458a036.

[24] D.D. Johnson, P. Singh, A.V. Smirnov, N. Argibay, Universal maximum strength of solid metals and alloys, Phys. Rev. Lett. 130 (2023) 166101, https://doi.org/10.1103/PhysRevLett.130.166101.

[25] S.L. Shang, A. Saengdeejing, Z.G. Mei, D.E. Kim, H. Zhang, S. Ganeshan, Y. Wang, Z.K. Liu, First-principles calculations of pure elements: equations of state and elastic stiffness constants, Comput. Mater. Sci. 48 (2010) 813–826, https://doi.org/10.1016/j.commatsci.2010.03.041.

[26] R. Tran, Z. Xu, B. Radhakrishnan, D. Winston, W. Sun, K.A. Persson, S.P. Ong, Surface energies of elemental crystals, Sci. Data 3 (2016) 160080, https://doi.org/10.1038/sdata.2016.80.

[27] A. Jain, S.P. Ong, G. Hautier, W. Chen, W.D. Richards, S. Dacek, S. Cholia, D. Gunter, D. Skinner, G. Ceder, K.A. Persson, Commentary: the Materials Project: a materials genome approach to accelerating materials innovation, Apl. Mater. 1 (2013) 011002, https://doi.org/10.1063/1.4812323.

[28] S.-L. Shang, M.C. Gao, D.E. Alman, Z.-K. Liu, Effect of hydrogen on surface energy of fcc Fe alloys: a first-principles study, Mater. Today Commun. 41 (2024) 110315, https://doi.org/10.1016/j.mtcomm.2024.110315.

[29] S.-L. Shang, B.-C. Zhou, W.Y. Wang, A.J. Ross, X.L. Liu, Y.-J. Hu, H.-Z. Fang, Y. Wang, Z.-K. Liu, A comprehensive first-principles study of pure elements: vacancy formation and migration energies and self-diffusion coefficients, Acta Mater. 109 (2016) 128–141, https://doi.org/10.1016/j.actamat.2016.02.031.

[30] Y. Wang, S. Curtarolo, C. Jiang, R. Arroyave, T. Wang, G. Ceder, L.Q. Chen, Z. K. Liu, Ab initio lattice stability in comparison with CALPHAD lattice stability, Calphad 28 (2004) 79–90.

[31] T. Zhu, J. Li, Ultra-strength materials, Prog. Mater. Sci. 55 (2010) 710–757. https://linkinghub.elsevier.com/retrieve/pii/S0079642510000265. (Accessed 30 July 2021).

[32] S. Zhang, X. Xu, T. Lin, P. He, Recent advances in nano-materials for packaging of electronic devices, J. Mater. Sci. Mater. Electron. 30 (2019) 13855–13868, https://doi.org/10.1007/s10854-019-01790-3.

[33] S.L. Shang, W.Y. Wang, Y. Wang, Y. Du, J.X. Zhang, A.D. Patel, Z.K. Liu, Temperature-dependent ideal strength and stacking fault energy of fcc Ni: a first-principles study of shear deformation, J. Phys. Condens. Matter 24 (2012) 155402, https://doi.org/10.1088/0953-8984/24/15/155402.

[34] S.L. Shang, W.Y. Wang, B.C. Zhou, Y. Wang, K.A. Darling, L.J. Kecskes, S. N. Mathaudhu, Z.K. Liu, Generalized stacking fault energy, ideal strength and twinnability of dilute Mg-based alloys: a first-principles study of shear deformation, Acta Mater. 67 (2014) 168–180, https://doi.org/10.1016/j.actamat.2013.12.019.

[35] Z. Han, H. Chen, X. Li, R. Jiang, S. Zhou, Novel application of MgH2/MoS2 hydrogen storage materials to thiophene hydrodesulfurization: a combined experimental and theoretical case study, Mater. Des. 158 (2018) 213–223, https://doi.org/10.1016/j.matdes.2018.08.036.

[36] H. Chen, P. Liu, J. Li, Y. Wang, C. She, J. Liu, L. Zhang, Q. Yang, S. Zhou, X. Feng, MgH2/Cu xO hydrogen storage composite with defect-rich surfaces for carbon dioxide hydrogenation, ACS Appl. Mater. Interfaces 11 (2019) 31009–31017, https://doi.org/10.1021/ACSAMI.9B11285/ASSET/IMAGES/LARGE/AM9B11285_0008.JPEG.

[37] H. Chen, N. Ma, C. Cheng, H. Zhang, W. Yuan, P. Liu, X. Feng, J. Liu, Q. Yang, S. Zhou, Hydrogen activation on aluminium-doped magnesium hydride surface for methanation of carbon dioxide, Appl. Surf. Sci. 515 (2020) 146038, https://doi.org/10.1016/j.apsusc.2020.146038.

[38] H. Chen, N. Ma, J. Li, Y. Wang, C. She, Y. Zhang, X. Li, J. Liu, X. Feng, S. Zhou, Effect of atomic iron on hydriding reaction of magnesium: atomic-substitution and atomic-adsorption cases from a density functional theory study, Appl. Surf. Sci. 504 (2020) 144489, https://doi.org/10.1016/j.apsusc.2019.144489.

[39] H. Chen, M. Zheng, J. Li, J. Liu, G. Zhou, X. Feng, Effect of surface carbon of iron carbide on Fischer-Tropsch synthesis: a density functional theory study, Int. J. Hydrogen Energy 86 (2024) 844–852, https://doi.org/10.1016/j.ijhydene.2024.08.504.

[40] J. Yao, B. Wang, H. Chen, Z. Han, Y. Wu, Z. Cai, G.W. Manggada, M.A. Elsayed, S. Zhou, Effect of copper cluster on reaction pathways of carbon dioxide hydrogenation on magnesium hydride surface, Int. J. Hydrogen Energy 78 (2024) 1089–1098, https://doi.org/10.1016/j.ijhydene.2024.06.382.

[41] H. Chen, H. Xiao, Y. Wang, J. Liu, Q. Yang, X. Feng, Insight into the energy conversion and structural evolution of magnesium hydride during high-energy ball milling for its controllable synthesis, J. Alloys Compd. 836 (2020) 155312, https://doi.org/10.1016/j.jallcom.2020.155312.

[42] X. Chong, S.-L. Shang, A.M. Krajewski, J.D. Shimanek, W. Du, Y. Wang, J. Feng, D. Shin, A.M. Beese, Z.-K. Liu, Correlation analysis of materials properties by machine learning: illustrated with stacking fault energy from first-principles calculations in dilute fcc-based alloys, J. Phys. Condens. Matter 33 (2021) 295702, https://doi.org/10.1088/1361-648X/ac0195.

[43] S.L. Shang, C.L. Zacherl, H.Z. Fang, Y. Wang, Y. Du, Z.K. Liu, Effects of alloying element and temperature on the stacking fault energies of dilute Ni-base superalloys, J. Phys. Condens. Matter 24 (2012) 505403, https://doi.org/10.1088/0953-8984/24/50/505403.

[44] N. Bernstein, E. Tadmor, Tight-binding calculations of stacking energies and twinnability in fcc metals, Phys. Rev. B 69 (2004) 094116, https://doi.org/10.1103/PhysRevB.69.094116.

[45] S.L. Shang, J. Shimanek, S. Qin, Y. Wang, A.M. Beese, Z.K. Liu, Unveiling dislocation characteristics in Ni3Al from stacking fault energy and ideal strength: a first-principles study via pure alias shear deformation, Phys. Rev. B 101 (2020) 024102, https://doi.org/10.1103/PhysRevB.101.024102.

[46] S. Ogata, J. Li, S. Yip, Ideal pure shear strength of aluminum and copper, Science 298 (2002) 807–811, https://doi.org/10.1126/science.1076652.

[47] M. Jahnatek, J. Hafner, M. Krajci, M. Jahnátek, J. Hafner, M. Krajčí, Shear deformation, ideal strength, and stacking fault formation of fcc metals: a density-functional study of Al and Cu, Phys. Rev. B 79 (2009) 224103. https://link.aps.org/doi/10.1103/PhysRevB.79.224103.

[48] C.R. Weinberger, B.L. Boyce, C.C. Battaile, Slip planes in bcc transition metals, Int. Mater. Rev. 58 (2013) 296–314, https://doi.org/10.1179/1743280412Y.0000000015.

[49] D. Roundy, C.R. Krenn, M.L. Cohen, J.W. Morris, The ideal strength of tungsten, Philos. Mag. A 81 (2001) 1725–1747, https://doi.org/10.1080/01418610108216634.

[50] K.A. Bukreeva, A.M. Iskandarov, S.V. Dmitriev, Y. Umeno, R.R. Mulyukov, Theoretical shear strength of FCC and HCP metals, Phys. Solid State 56 (2014) 423–428, https://doi.org/10.1134/S1063783414030081, 2014 563.

[51] P. Garg, M.A. Bhatia, K.N. Solanki, Uncovering the influence of metallic and non-metallic impurities on the ideal shear strength and ductility of Ti: an ab-initio study, J. Alloys Compd. 788 (2019) 413–421, https://doi.org/10.1016/J.JALLCOM.2019.02.231.

[52] A. van de Walle, P. Tiwary, M. de Jong, D.L. Olmsted, M. Asta, A. Dick, D. Shin, Y. Wang, L.-Q. Chen, Z.-K. Liu, Efficient stochastic generation of special quasirandom structures, Calphad 42 (2013) 13–18, https://doi.org/10.1016/j.calphad.2013.06.006.

[53] T. Bučko, J. Hafner, J.G. Ángyán, Geometry optimization of periodic systems using internal coordinates, J. Chem. Phys. 122 (2005) 124508, https://doi.org/10.1063/1.1864932.

[54] G. Kresse, J. Furthmüller, Efficient iterative schemes for *ab initio* total-energy calculations using a plane-wave basis set, Phys. Rev. B 54 (1996) 11169–11186, https://doi.org/10.1103/PhysRevB.54.11169.

[55] G. Kresse, D. Joubert, D. Kresse, G. Joubert, From ultrasoft pseudopotentials to the projector augmented-wave method, Phys. Rev. B 59 (1999) 1758–1775, https://doi.org/10.1103/PhysRevB.59.1758.

[56] J.P. Perdew, K. Burke, M. Ernzerhof, Generalized gradient approximation made simple, Phys. Rev. Lett. 77 (1996) 3865–3868, https://doi.org/10.1103/PhysRevLett.77.3865.

[57] J.D. Shimanek, S.-L. Shang, A.M. Beese, Z.-K. Liu, Insight into ideal shear strength of Ni-based dilute alloys using first-principles calculations and correlational analysis, Comput. Mater. Sci. 212 (2022) 111564, https://doi.org/10.1016/j.commatsci.2022.111564.

[58] G.V. Samsonov, Handbook of the Physicochemical Properties of the Elements, Springer, New York, 1968, https://doi.org/10.1007/978-1-4684-6066-7_1.

[59] AZOM Materials, (n.d.). https://www.azom.com/(accessed October 23, 2023).

[60] J.M. Wheeler, R. Raghavan, J. Wehrs, Y. Zhang, R. Erni, J. Michler, Approaching the limits of strength: measuring the uniaxial compressive strength of diamond at small scales, Nano Lett. 16 (2016) 812–816, https://doi.org/10.1021/acs.nanolett.5b04989.

[61] S. Ogata, J. Li, N. Hirosaki, Y. Shibutani, S. Yip, Ideal shear strain of metals and ceramics, Phys. Rev. B 70 (2004) 104104, https://doi.org/10.1103/PhysRevB.70.104104.

[62] J.W. Morris, C.R. Krenn, D. Roundy, M.L. Cohen, Deformation at the limit of elastic stability, Mater. Sci. Eng., A 309–310 (2001) 121–124, https://doi.org/10.1016/S0921-5093(00)01735-4.

[63] D.H. Chung, W.R. Buessem, The voigt-reuss-hill approximation and elastic moduli of polycrystalline MgO, CaF2, β-ZnS, ZnSe, and CdTe, J. Appl. Phys. 38 (1967) 2535–2540, https://doi.org/10.1063/1.1709944.

[64] K.M. Knowles, P.R. Howie, The directional dependence of elastic stiffness and compliance shear coefficients and shear moduli in cubic materials, J. Elasticity 120 (2015) 87–108, https://doi.org/10.1007/s10659-014-9506-1.

[65] C.R. Krenn, D. Roundy, J.W. Morris, M.L. Cohen, Ideal strengths of bcc metals, Mater. Sci. Eng., A 319–321 (2001) 111–114, https://doi.org/10.1016/S0921-5093(01)00998-4.

[66] Y.-J. Hu, A. Sundar, S. Ogata, L. Qi, Screening of generalized stacking fault energies, surface energies and intrinsic ductile potency of refractory multicomponent alloys, Acta Mater. 210 (2021) 116800, https://doi.org/10.1016/j.actamat.2021.116800.